

Journal of Materials Chemistry A

Accepted Manuscript



This is an *Accepted Manuscript*, which has been through the Royal Society of Chemistry peer review process and has been accepted for publication.

Accepted Manuscripts are published online shortly after acceptance, before technical editing, formatting and proof reading. Using this free service, authors can make their results available to the community, in citable form, before we publish the edited article. We will replace this *Accepted Manuscript* with the edited and formatted *Advance Article* as soon as it is available.

You can find more information about *Accepted Manuscripts* in the [Information for Authors](#).

Please note that technical editing may introduce minor changes to the text and/or graphics, which may alter content. The journal's standard [Terms & Conditions](#) and the [Ethical guidelines](#) still apply. In no event shall the Royal Society of Chemistry be held responsible for any errors or omissions in this *Accepted Manuscript* or any consequences arising from the use of any information it contains.

Cite this: DOI: 10.1039/c0xx00000x

www.rsc.org/xxxxxx

ARTICLE TYPE

High Lithium Electroactivity of Boron-doped Hierarchical Rutile Submicrospheres TiO₂

Huajun Tian, Fengxia Xin, Xiaojian Tan and Weiqiang Han*

Received (in XXX, XXX) Xth XXXXXXXXX 20XX, Accepted Xth XXXXXXXXX 20XX

DOI: 10.1039/b000000x

We have reported a facile method to fabricate hierarchical boron-doped rutile submicrospheres TiO₂ (SMT), whose primary particles are ~20nm diameter. The as-synthesized boron-doped SMT shows excellent cycling performance and rate capability in comparison with undoped TiO₂ as an anode material in Lithium-ion Batteries (LIBs). It has a very stable capacity of ~190 mAh/g for 500 cycles at 1C. In addition, the density functional theory (DFT) calculations are carried out to indicate that the low concentration (< 1.0 at.%) of boron doping could enhance the carrier mobility μ and electrical conductivity σ , and thus reveal the relationship between the electronic structure of boron-doped SMT and the performances of boron-doped SMT anode in LIBs. Our results also clearly demonstrate the importance and advantage of the hierarchical submicrometer-sized spherical morphology of TiO₂ anode in LIBs.

Introduction

Micro(nano)-structure materials have attracted great interests because of their promising applications in a wide range of areas, such as dye-sensitized solar cells^{1, 2}, photocatalysis for degradation of organic pollutants^{3, 4}, photoelectrochemical splitting of water into hydrogen and oxygen⁵, lithium-ion batteries (LIBs)^{6, 7} et.al. As one of the most promising energy-storage solution, rechargeable lithium-ion batteries have been widely used in portable electronics and are promising for applications in electric vehicles (EVs), hybrid electric vehicles (HEVs) and smart grids⁸. Nevertheless, it is still a major challenge to develop new materials with high energy density, long cycle life, excellent rate capability performance, and environmental compatibility. Therefore, safe, nontoxic, and high rate capable electrode materials present significant role in LIBs. As an anode material, micrometer-sized morphology is provided a step forward by assuring high tap density as well as high volumetric capacity.⁹ On the other hand, micrometer-sized particles of electrode are generally affected by a long Li⁺ ion diffusion path, which results in a poor rate capability. Reduction of the particles to a nanometer-size dimension could significantly reduce the Li⁺ diffusion path and increase the contact area with the electrolyte.¹⁰ However, nanoparticles materials as anodes in the circling tend to self-aggregate, which shorten the effective contact areas among the active materials, conductive reagent, and electrolyte.¹¹ Most encouragingly, hierarchical structure has aroused much interest in a variety of field because of their extraordinarily high active surface/interface and robust stability.^{12, 13} Although significant advancement has been achieved by engineering electrode structure and morphology, further improvement (i.e., the more simple preparation method, the higher stability, and the better rate capability, et al.) is still required.

Titanium dioxide (TiO₂), is a good candidate for anode materials in view of its properties such as low cost, environmental friendliness, higher Li-insertion potential (1.5–1.8 V vs. Li⁺/Li) than the commercialized carbon anode materials, and thereby is safe by avoiding Li electroplating.¹⁴ Recently, a variety of TiO₂ polymorphs have been used as efficient anodic materials in LIBs, including rutile¹⁵, anatase¹⁶, brookite¹⁷, TiO₂(B)^{18, 19} and Magnéli phase Ti_nO_{2n-1}.²⁰ Besides, rutile is the thermodynamically most stable structure of TiO₂, and is also the most common natural form. A lot of efforts have been devoted to understand the nature of lithium insertion into the rutile crystal structure.^{8, 15, 21} Nevertheless, the nearly one-dimensional diffusion of Li-ions in rutile TiO₂ restrains the application of bulk rutile TiO₂ as anode in LIBs. However, it has been demonstrated that lithium can be reversibly inserted into the nanosized rutile TiO₂.²² Moreover, the main bottleneck is the low electronic conductivity of TiO₂ (including the rutile TiO₂) and the low diffusivity of Li-ions in TiO₂, which is governed by ambipolar transport. Up to now, the main approaches for improving the electronic and ionic charge transport of TiO₂ electrodes conclude: i) adding conductive additives such as carbon (including carbon coating) for increasing the electronic conductivity²³; ii) reducing the TiO₂ particle size for providing more 3D Li-ion diffusion pathway²⁴; iii) substitutional doping of TiO₂ with heteroatom for enhancing the electronic conductivity²⁵⁻²⁸. The hierarchical structure materials without a carbon coating have always been greatly attractive but very challenging. Doping technique (i.e., P-type or N-type doping) for TiO₂, which is attributed to an increase in donor density, is also a facile strategy to design an efficient anode structure.^{10, 27, 29-31} Ali et al. prepared Zn doped mesoporous TiO₂ microspheres as anode in LIBs, indicating that its superior rate performance could be attributed to enhanced electronic and ionic conductivity.²⁷ Meanwhile, the doping

benefits charge transfer, and a slight modification in the TiO₂ lattice may offer more open channels in a particular direction for Li-ion diffusion. Kim et al. reported the nitrogen doping on the lithium storage properties of TiO₂ in rechargeable batteries. The results indicated that the nitrogen interstitially located near surface in the form of TiO₂N_x, improving the conductivity and Li⁺ diffusion.³² Ventosa et al. indicated that the creation of oxygen vacancies upon ammonia annealing is the main reason for the improvement of the stability and C-rate performance for N-doped TiO₂ as anode in LIBs.³⁰ In the Doping techniques for TiO₂, the boron doping in TiO₂ has been widely investigated in many fields, such as photocatalysis, dye-sensitized solar cells et al.^{33, 34} Gopal et al. also proposed that boron doping favors formation of an oxygen vacancy with two excess electrons, which would further reduce two Ti⁴⁺ ions to form Ti³⁺.³⁵ The conductivity of TiO₂ increases with increasing concentration of oxygen vacancies in rutile single crystals.^{36, 37} However, the boron doping on the TiO₂ as anode in LIBs has not been researched. Therefore, this work gave an insight in investigating on the boron doping in hierarchical TiO₂ as a potential anode in LIBs.

Herein, we fabricated a hierarchical boron-doped rutile submicrospheres TiO₂ without carbon coating, which consisted on the TiO₂ nanoparticles with an average diameter of ~20nm. In this study, electronic transport in rutile TiO₂ has been investigated in detail using density functional theory (DFT) calculations, in order to gain insights from the atomistic details of low concentration boron doping in TiO₂ that could influence its performance as a prospective LIBs electrode. The results exhibit the excellent electrochemical performance of hierarchical boron-doped rutile submicro-sphere TiO₂, which shows the high capacity and stable cyclability under the fast charge/discharge rate.

Experimental details of boron-doped submicrospheres TiO₂ preparation

The samples were synthesized via a modified solvothermal method.³⁸ An appropriate amount of boric acid was dissolved in 30 mL of deionized water prior to hydrolysis of titanium tetrachloride (Aldrich) under vigorous stirring. A required amount of high purity TiCl₄ was added drop wise to 50 ml absolute ethanol. To the homogeneous solution obtained in this stage was added into a calculated quantity of boric acid solution above mentioned with continuous stirring. Absolute ethanol was added to control the rate of hydrolysis process at a temperature of 60 °C for 12 h. After the reaction was completed, the resultant slurry was filtered and washed three times with absolute ethanol and deionized water. The powder samples obtained were vacuum-dried and sintered at 510 °C for 10 h in air. Scheme 1 shows the procedure for the preparation of boron-doped submicrospheres TiO₂. The XRD patterns and particle sizes of the different samples sintered at various temperatures were presented in Fig. S1 and Table S1 (ESI †). At the higher calcination temperatures, the crystallites formed are larger in size.

Structural Characterizations

XRD measurements were performed on a D8 Diffractometer from Bruker instruments (Cu K α radiation= 0.154 nm) equipped

with a scintillation counter. The samples were characterized using scanning electron micro-copy (FESEM and HR-SEM, Hitachi, S-4800) and transmission electron microscopy (TEM, FEI Ltd., Tecnai F20). The interstitial and substitution of the oxygen sites with boron atoms in the titania structure was confirmed by X-ray photoelectron spectroscopy (XPS, Shimadzu group company, Japan). The BET specific surface area and pore size and volume were analyzed using N₂ absorption on an ASAP 2020M (Micromeritics Instrument Corp., USA).

Electrochemical Measurements

The boron-doped submicrospheres TiO₂ was mixed with Super P carbon black and polyvinylidene fluoride (PVDF) to form slurry at the weight ratio of 70:20:10. The Super P carbon black additive did not contribute to the total capacity as it acted only as a conducting agent. The electrode was prepared by casting the slurry onto copper foil with active material loading of ~1.5 mg/cm² using a doctor blade and dried in a vacuum oven at 120 °C overnight. The CR2032 coin cells were assembled with lithium foil as the counter electrode, 1.0 M LiPF₆ solution in a mixture of ethylene carbonate/diethyl carbonate (EC/DEC, 1:1 by volume) as the electrolyte, and a polypropylene film (Celgard-2300) was used as a separator. The coin cells were assembled in an argon-filled glove box. The electrochemical properties were studied with a multichannel battery-testing system (BT2000, Arbin Instruments, USA). Capacity was calculated on the basis of the total mass of the boron-doped submicrospheres TiO₂. Rate capability was examined by charging and discharging cells at different rates from 0.5C to 10C. All the capacities and rate performance were calculated based on TiO₂ active materials (1C corresponding to 335 mAh/g). Cyclic voltammogram scanned at 0.02 mV/s between 1.0~3.0 V for 5 cycles was recorded using Solatron 1260/1287 Electrochemical Interface (Solartron Metrology, UK). EIS was taken using a Solatron 1260/1287 Electrochemical Interface (Solartron Metrology, UK) electrochemical workstation at 25 °C with the frequency ranging from 1 MHz to 0.001Hz and an AC signal of 10 mV in amplitude as the perturbation.

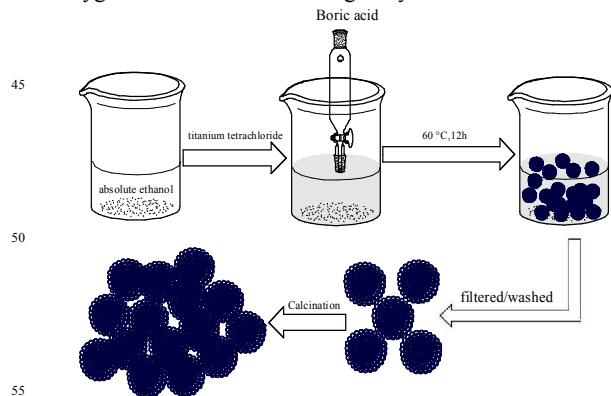
Electronic structure calculation

The electronic structure calculations have been performed using a first-principle plane-wave pseudopotential formulation within the framework of density functional theory (DFT)³⁹⁻⁴¹. The exchange-correlation energy is in the form of Perdew-Burke-Ernzerhof (PBE) with generalized gradient approximation (GGA)⁴². Projector-augmented wave (PAW) potentials are used for the Ti, O, and B atoms and the cutoff energy is set as 400 eV. During the geometry optimizations, both the atomic positions and the lattice constants are fully relaxed until the magnitude of the force acting on all atoms becomes less than 0.01 eV/Å, which also converge the total energy within 1 meV. In order to achieve a doping level as low as 0.5 atom %, the rutile TiO₂ are modeled by an orthometric 4×4×2 supercell which contains 64 Ti and 128 O atoms.

Results and discussion

The boron-doped submicrospheres titania were prepared by a facile hydrothermal synthesis method. A schematic of the

procedure for the samples preparation is shown in Scheme 1. Fig. 1(a) is the image of the powder obtained at 510 °C for 10 h in air, which was denoted as boron-doped submicrospheres titania (B-doped SMT). The SEM image shows the submicrospheres-like morphology, in which the diameter of the sample varies from 600 nm to 650 nm. Meanwhile, the B-doped SMT sample has a very rough surface, which consists of 18~23 nm size nanoparticles. It could be confirmed by TEM and HRTEM (Fig.1b and 1c). The TEM images present the B-doped SMT samples containing nanocrystals (~20 nm). Well-ordered diffraction rings are noted in the selected area electron diffraction (SAED) pattern (Inset of Fig.1d). It demonstrates that the B-doped SMT is polycrystalline. According to the X-ray diffraction pattern (XRD) shown in Fig.1e, the sample exhibits the characteristic diffraction peaks at 27.45°, 36.09°, 39.19°, 41.23°, 44.05°, 54.32°, 56.64°, 62.74°, 64.04°, 65.48°, 69.01°, 69.79°, 72.41°, 74.41°, 76.51°, 79.82°, respectively, which can be indexed to the (110), (101), (200), (111), (210), (211), (220), (002), (310), (221), (301), (112), (311), (320), (202), (212) planes of rutile TiO₂ (JCPDS:21-1276) without any other secondary phases such as anatase and brookite. The corresponding X-ray photoelectron spectroscopy (XPS) pattern recorded from the boron-doped SMT is shown in Fig.1f. It could be observed that there is one main peak at 188.0 eV for B 1s. In the previous studies, the B-doped TiO₂ often exhibits a peak of the B 1s level about 192 eV. The standard binding energy of B 1s in boron oxide, B₂O₃, is around 194 eV.⁴³⁻⁴⁵ In some cases, the B 1s peak around 192 eV coexists with other peaks at higher binding energies, indicating the possible formation of B₂O₃ into or at the surface of the titania structure, while in TiB₂ the B 1s level shifts to smaller binding energies, about 188 eV.⁴³ The absence of the peak at 194 eV in Figure 1f is the signature of the fact that B has entered into the structure as a diluted impurity.⁴⁶ In the B1s XPS spectra, the maximum amount of the B in the B-doped TiO₂ sample was estimated at about 0.71 at.% (< 1 at. %). The main signal peak at 188.0 eV observed should be attributed to the B-Ti-B. Therefore, the XPS indicated that the signal peak in Figure 1f was ascribed to the substitutional boron for the oxygen. It was proposed that boron doping favors formation of an oxygen vacancy with two excess electrons, which would further reduce two Ti⁴⁺ ions to form Ti³⁺.³⁵ Meanwhile, the conductivity of TiO₂ increases with the increasing concentration of oxygen vacancies in rutile single crystals.^{36, 37}



Scheme 1. Schematic diagram of preparation process for boron-doped SMT.

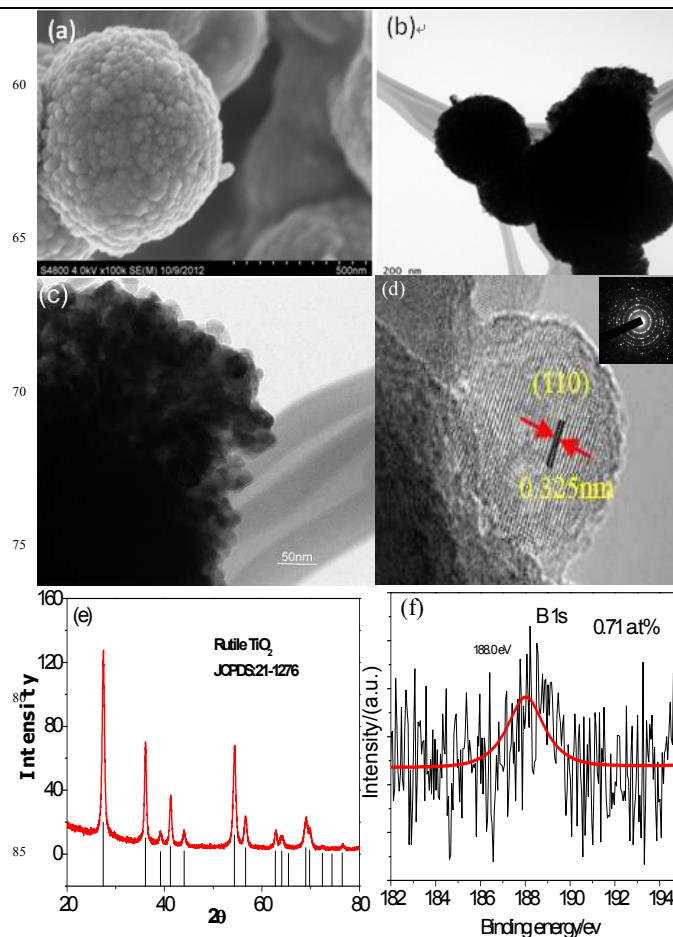


Figure 1 (a) High magnification SEM image of boron-doped SMT; (b), (c) TEM and (d) HRTEM images of the boron-doped SMT. Inset of (d) the selected area electron diffraction (SAED) patterns of SMT sample; (e) XRD pattern of the boron-doped SMT sample; (f) High-resolution X-ray photoelectron spectroscopy (XPS) pattern of the boron-doped SMT.

A fundamental understanding of the electrical properties in doped TiO₂ is important. To investigate the influence of boron doping on the electrical conductivity, we investigated the influences of O atoms substituted by B atoms using density functional theory (DFT). And the atomic ratio were defined 0.5 at.% and 1.0 at.%, respectively. The relaxed lattice constants *a* and *c* of rutile TiO₂ are 4.593 and 2.959 Å, respectively. These values are very close to those found experimentally.⁴⁷ Figure 2(i) shows the calculated density of state (DOS) of pure and boron-doped rutile TiO₂ samples, it can be seen that B-doping moves the Fermi level toward the conduction band (CB), thus the main carriers in these structures are electron. According to the equation $\sigma = ne\mu$, high electrical conductivity σ needs high carrier concentration *n* and high carrier mobility μ . The carrier (electron) concentration *n* can be obtained by integrating the DOS between the band gap and the Fermi level. Considering the carrier mobility is inverse proportional to the defect concentration *N* and effective mass *m*^{*}, the relationship between σ , *n*, *N*, and *m*^{*} can be expressed as $\sigma \propto n/Nm^*$. We also calculated the band structure of the supercell of boron-doped rutile TiO₂ (Fig.2(ii)) and studied the effective mass at the conduction band minimum (CBM)

according to $m^* = \hbar^2 / [\partial^2 \varepsilon(k) / \partial k^2]$, where \hbar is the reduced Planck constant. These parameters are listed in Table 1, it can be seen that as the B-doping level (< 1.0 at. %) increased from 0.5 at. % to 1.0 at. %, both carrier concentration n and defect concentration N are increased while effective mass m^* is decreased, leading to the enhanced carrier mobility μ and electrical conductivity σ . Thus, the low concentration of boron doping could enhance the carrier mobility μ and electrical conductivity σ .

Figure 3 illustrates the adsorption-desorption isotherm and the pore size distribution analyzed by the Barrett-Joyner-Halenda (BJH) method. In Fig. 3a, the Brunauer-Emmett-Teller (BET) specific surface area of the boron-doped SMT is 22.5 m²/g and the pore volume is ~ 0.1 cm³/g. The BJH pore size distribution curve in Fig. 3b exhibited a narrow pore size distribution, with average pore diameters around 18 nm. The mesoporous structure of boron-doped SMT provides an enhanced contact area between electrode and electrolyte, and facilitates the lithium transportation during cycling.⁴⁸

Figure 4a shows the cycle performance of the boron-doped SMT between 3.0 V and 1.0 V in the electrolyte of 1 M LiPF₆/EC (ethylene carbonate) + DEC (diethyl carbonate). The cycling performance of boron-doped SMT was evaluated at 0.5C, 1C and 2C. As shown in Fig. 4a, the boron-doped SMT shows excellent cyclability with higher capacity compared with the undoped TiO₂ anode (Inset of Fig. 4a). A capacity of ~ 190 mAh/g at 1C was retained after 500 cycles of full charge/discharge, which is much higher than the undoped TiO₂ anode. In contrast, the undoped TiO₂ drops to around ~ 108 mAh/g after 120 cycles (Inset of Fig. 4a). Meanwhile, the boron-doped SMT anode could remain the capacity of ~ 146 mAh/g at 2C after another 300 cycles in

Table 1: Calculated carrier concentration n , defect concentration N , and effective mass m^* for 0.5 at. % and 1.0 at. % B-doped rutile TiO₂.

B-doping	n (/cm ³)	N (/cm ³)	m^* (m_e)	μ'	σ'
0.5 at. %	1.502×10^{21}	5×10^{20}	5.755	0.347	0.522
1.0 at. %	2.002×10^{21}	1×10^{21}	1.989	0.503	1.007

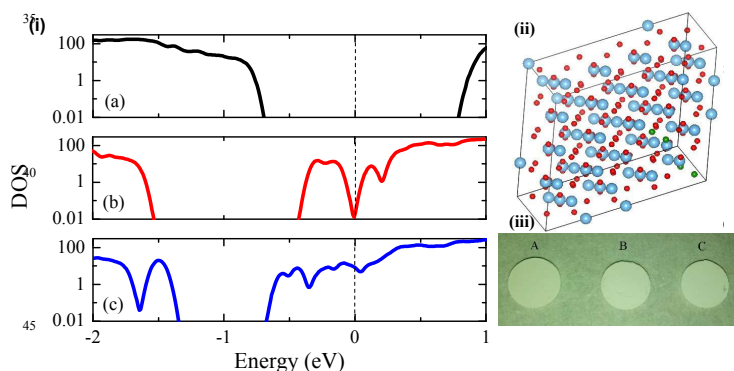


Figure 2. (i) Calculated density of state (DOS) of 4x4x2 rutile TiO₂ supercell: (a) pure, (b) 0.5 at. % B-doped and (c) 1.0 at. % B-doped. (ii) supercell of boron-doped rutile structures. O atoms are shown as red spheres, Ti atoms are shown as light blue spheres, B atoms are shown as green spheres (iii) photographs of (A) pure TiO₂, (B) submicrospheres TiO₂ and (C) boron-doped submicrospheres TiO₂.

Fig. 4a. The results show that the boron-doped SMT anode exhibits the higher reversible capacity and better cycling performance. Cyclic voltammetry has been carried out between 0–3.0 V on rutile boron-doped SMT at a scan rate of 0.02 mV/s for 5 cycles. The obtained voltammograms are presented in Fig. 4b. The first cycle between 1.0 and 3.0 V shows two cathodic peaks at 1.27 and 1.11V. These peaks are ascribed to an irreversible phase transformation from TiO₂ to LiTiO₂.⁴⁹ The subsequent cycles show reduction and oxidation peaks at about 1.8 V, which are consistent with lithium insertion/extraction in LiTiO₂.⁵⁰ An increase of the intensity of these current peaks upon cycling can be observed in Fig. 4b indicating the excellent kinetics. To further confirm the excellent performance of the boron-doped SMT electrode, the electrochemical properties of boron-doped SMT electrode were studied by charge/discharge at different C rates between 1.0 and 3.0 V versus Li/Li⁺ ranging from 0.5C to 10C. The boron-doped SMT anode material exhibits an outstanding performance at C-rate test. In Fig. 4c and Fig. 4d, it can be seen that the capacities of boron-doped SMT at cycling rates of 0.5C, 1C, 2C, 5C, 10C were around 166 mAh/g (0.5C), 141 mAh/g (1C), 126 mAh/g (2C), 94 mAh/g (5C) and 72 mAh/g (10C), respectively. The most advantage for boron-doped SMT anode is the rate capability and cycling performance at high rates (10C) shown in Fig. 4c and 4d. Importantly, the capacity is then reversibly back to 167 mAh/g after 120 circles at different C rates, once the charging/discharging rate was set back to 0.5C again. Besides a good cycling stability, the boron-doped SMT sample also displays a rather high Columbic efficiency of near 100%, indicating an excellent electrochemical reversibility during cycling. The good electrochemical performance of boron-doped SMT can be attributed to the unique hierarchical submicrospheres structure and enhanced electronic conductivity by boron doping.

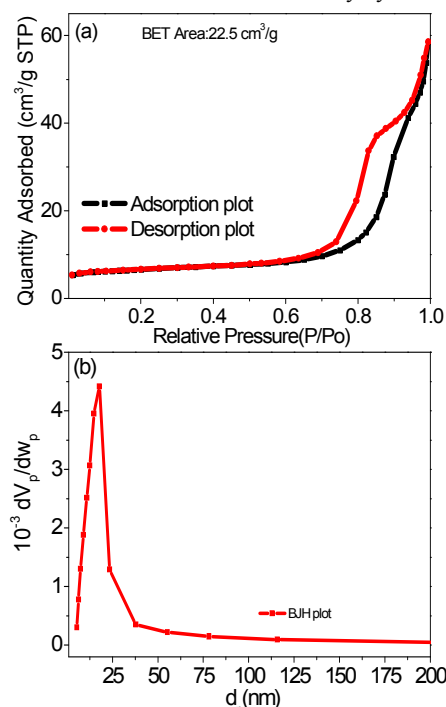


Figure 3. Nitrogen adsorption-desorption isotherms (a) and pore size distribution (b) of boron-doped SMT.

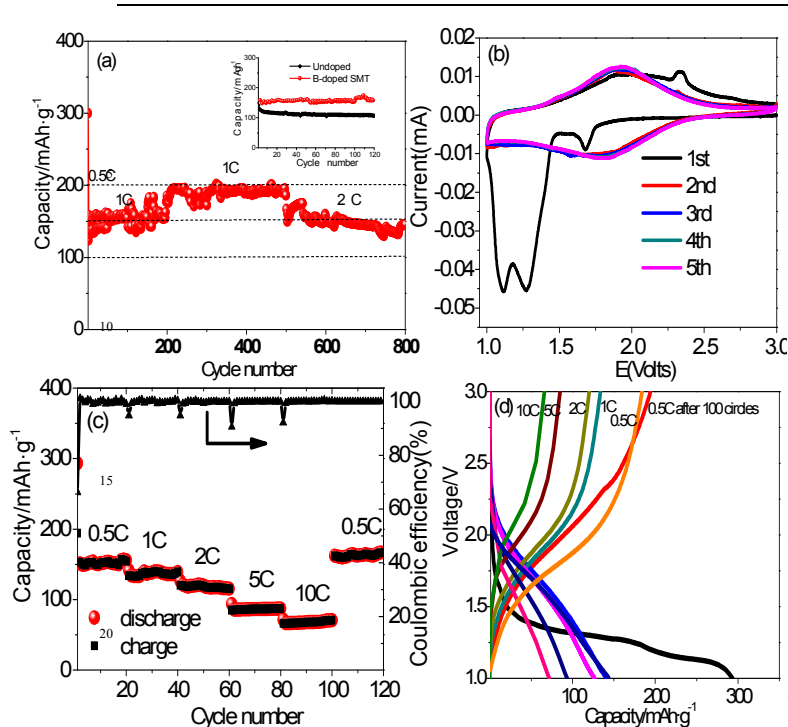


Figure 4. (a) Cycling behaviors of boron-doped SMT between 1.0 and 3.0 V. (b) Cyclic voltammograms of the initial 5 cycles of the boron-doped submicrospheres TiO_2 . (c) Rate capacity of the boron-doped SMT between 1.0 and 3.0 V at various rates (0.5C-10C). (d) charge/discharge profiles of the boron-doped SMT at different rates from 0.5 C to 10 C.

To further investigate the mechanisms contributing to superior rate capability of the boron-doped SMT, the detailed reaction kinetics of the boron-doped submicrospheres TiO_2 in LIBs were investigated using electrochemical impedance spectroscopy (EIS). The frequency range was set between 1 MHz and 1 mHz, and EIS was carried out on the sample after being discharged to 1 V at 1C in the 20th, 200th and 1000th cycle with a subsequent relaxation period of 2h, respectively. Interestingly, the impedance spectra are composed of two partially overlapped semicircles in the high-to-middle frequency range and a straight slopping line at low frequencies (Fig.5). The two partially overlapped semicircles in the high-to-middle frequency range is associated with two interface impedances (i.e., SEI or contact problems and charge-transfer impedance), and the low-frequency line corresponds to ion diffusion.⁵¹ The Nyquist plots obtained were modeled and interpreted with the help of an appropriate electric equivalent circuit shown in the Inset of Fig.5. The R_{ct} decreased from 696.3 Ω to 259.4 Ω in Nyquist plots for the boron-doped SMT anode after 20, 200 and 1000 cycles, displaying a depressed semicircle in the high-middle frequency region and an oblique straight line in the low frequency region. Impressively, there is even a slight decrease in charge-transfer resistance after 1000 discharge/charge cycles, indicating the good stability of the as-prepared electrodes. These plots with small semicircle diameters in the high-to-middle frequency range suggest that the electrodes possess low contact and charge-transfer impedances.

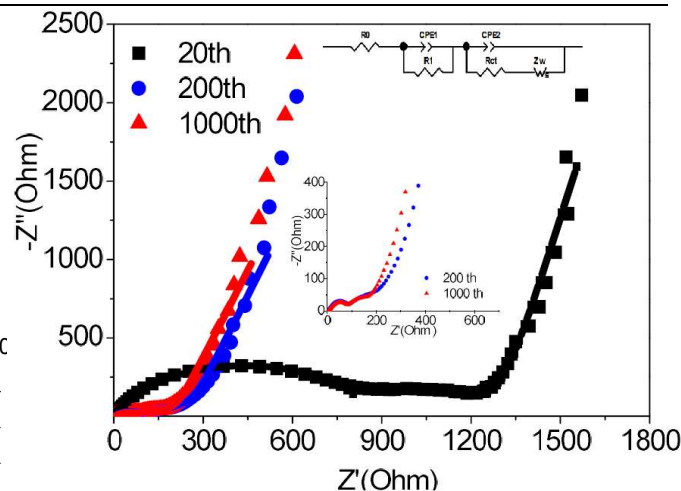


Figure 5. Nyquist plots of the electrodes of boron-doped SMT after 20, 200 and 1000 charge/discharge cycles at 1C rate, obtained after discharge the boron-doped SMT anode to 1.0 V. Inset shows enlarged spectra at high-to-middle frequency range (Z' and Z'' denote real and imaginary parts, respectively). The lines show the fitted results in Nyquist plots.

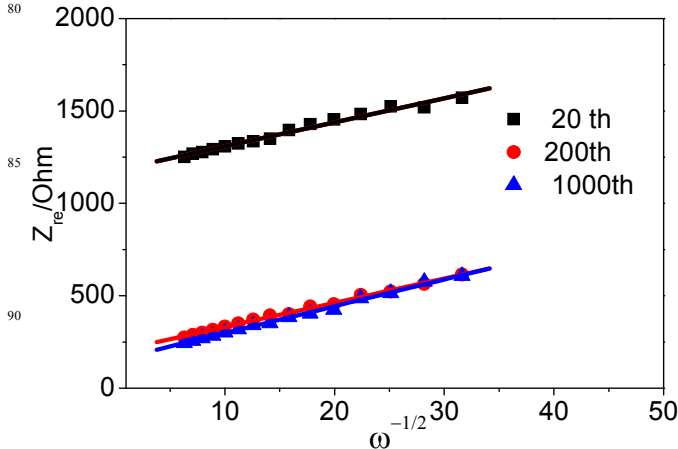


Figure 6. The relationship between Z_{re} and $\omega^{-1/2}$ at low-frequency region of boron-doped SMT after 20, 200 and 1000 charge/discharge cycles at 1C rate.

At the same time, we could investigate the Li^+ diffusion kinetics in the boron-doped SMT during the long-term charge/discharge process. The diffusion coefficient of lithium ion is calculated according to the equation (1)⁵²:

$$D_{Li} = \frac{R^2 T^2}{2n^4 F^4 A^2 \sigma^2 C_{Li}^2} \quad (1)$$

where the meanings of R is the gas constant, T is the absolute temperature, n is the number of electrons per-molecule during oxidation, D_{Li} is the diffusion coefficient of lithium ion, F is the Faraday constant, A is the surface area of the anode, C_{Li} is the concentration of lithium ion, and σ is the Warburg factor which has relationship with Z_{re} (equation (2))^{52, 53}:

$$Z_{re} = R_D + R_L + \sigma \omega^{-1/2} \quad (2)$$

The Figure 6 shows the relationship between Z_{re} and square root of frequency ($\omega^{-1/2}$) in the low-frequency region. It is conclude that, at 1C after 200 and 1000 cycles, the Li^+ insertion kinetics in

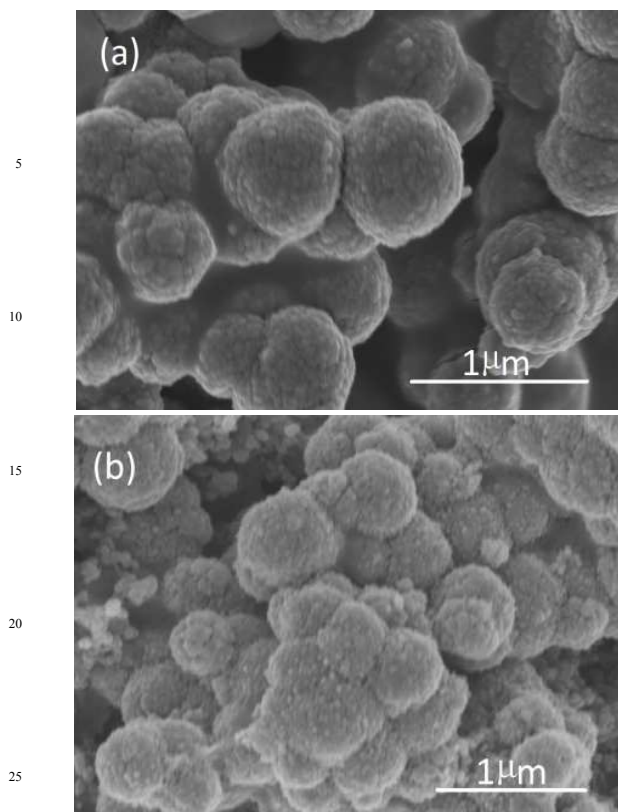


Figure 7. SEM images of the boron-doped SMT before (a) and after (b) 1000 charge/discharge cycles.

rutile boron-doped SMT anode were even a little better than the anode at the beginning of 20 cycles. The Li^+ insertion kinetics keep quite stable. The results could be attributed that the unique hierarchical submicrometer-sized spherical morphology and structural stability in rutile boron-doped SMT.

In comparison to the morphology of the fresh boron-doped SMT anode in Fig.7a, no obvious morphology change in aged boron-doped SMT anode (Fig.7b) was observed after 1000 charge/discharge cycles. In Figure 7b, we observed that the anode after 1000 cycles still almost retained the submicrospheres structure morphology, indicating that the boron-doped SMT could guarantee the enough contact areas among the active materials, conductive reagent, and electrolyte during the long-term charge/discharge process, which was responsible for the high capacity, long cycle life and excellent rate capability performance. The stability of the hierarchical submicrometer-sized spherical morphology would facilitate the lithium-ion transportation in the charge/discharge process.

Conclusions

In conclusion, hierarchical submicrospheres rutile TiO_2 have been synthesized by a facile solvothermal method and successfully employed as an anode material for lithium ion batteries. Boron doping was adopted to modify submicrosphere TiO_2 to make it electronically more conductive. In addition, the density functional theory (DFT) calculations are carried out to indicate that the low concentration (< 1.0 at.%) of boron doping could enhance the

carrier mobility μ and electrical conductivity σ . The hierarchical boron-doped SMT rutile TiO_2 exhibits excellent reversibility and stability. A highly stable capacity of 190 mAh/g remained after 500 circles at 1C. The good performance of boron-doped SMT is attributed to: (i) the unique hierarchical submicrospheres structure and (ii) enhanced carrier mobility μ and electrical conductivity σ . We believe that the high-performance boron-doped SMT will have wide applications in other fields such as photocatalysis and dye-sensitized solar cells.

Acknowledgements

This work was financially supported by the ‘‘Strategic Priority Research Program’’ of the Chinese Project Academy of Science (Grant No. XDA01020304), the National Natural Science Foundation of China (Grant No. 51371186), Ningbo 3315 International Team of Advanced Energy Storage Materials, Zhejiang Province Key Science and Technology Innovation Team, China Postdoctoral Science Foundation funded project (Grant No. 2013M541807) and Zhejiang Province Preferential Postdoctoral Funded Project (No. BSH1302055).

Notes and references

Ningbo Institute of Materials Technology & Engineering, Chinese Academy of Sciences,

No. 1219 Zhongguan West Road, Zhenhai District, Ningbo, Zhejiang 315201 P.R.China. Fax: +86-574-87615697; Tel: +86-574-87615697; E-mail: hanweiqiang@nimte.ac.cn

† Electronic Supplementary Information (ESI) available: [details of any supplementary information available should be included here]. See DOI: 10.1039/b000000x/

- U. Bach, D. Lupo, P. Comte, J. E. Moser, F. Weissortel, J. Salbeck, H. Spreitzer and M. Gratzel, *Nature*, 1998, **395**, 583-585.
- I. Chung, B. Lee, J. Q. He, R. P. H. Chang and M. G. Kanatzidis, *Nature*, 2012, **485**, 486-U494.
- S. Wang, T. Wang, W. X. Chen and T. R. Hori, *Chem Commun*, 2008, 3756-3758.
- C. Sarantopoulos, E. Puzenat, C. Guillard, J. M. Herrmann, A. N. Gleizes and F. Maury, *Appl Catal B-Environ*, 2009, **91**, 225-233.
- J. H. Park, S. Kim and A. J. Bard, *Nano Lett*, 2006, **6**, 24-28.
- J. M. Li, W. Wan, F. Zhu, Q. Li, H. H. Zhou, J. J. Li and D. S. Xu, *Chem Commun*, 2012, **48**, 389-391.
- D. H. Wang, D. W. Choi, J. Li, Z. G. Yang, Z. M. Nie, R. Kou, D. H. Hu, C. M. Wang, L. V. Saraf, J. G. Zhang, I. A. Aksay and J. Liu, *ACS Nano*, 2009, **3**, 907-914.
- A. S. Arico, P. Bruce, B. Scrosati, J. M. Tarascon and W. Van Schalkwijk, *Nat Mater*, 2005, **4**, 366-377.
- Y. K. Sun, S. M. Oh, H. K. Park and B. Scrosati, *Adv Mater*, 2011, **23**, 5050-5054.
- C. Lai, X. C. Yuan, X. L. Cao, Q. Q. Qiao, Y. L. Wang and S. H. Ye, *Electrochim Solid St*, 2012, **15**, A65-A67.
- P. G. Bruce, B. Scrosati and J. M. Tarascon, *Angew Chem Int Edit*, 2008, **47**, 2930-2946.
- L. C. Yang, S. N. Wang, J. J. Mao, J. W. Deng, Q. S. Gao, Y. Tang and O. G. Schmidt, *Adv Mater*, 2013, **25**, 1180-1184.

13. X. L. Wang, W. Q. Han, H. Y. Chen, J. M. Bai, T. A. Tyson, X. Q. Yu, X. J. Wang and X. Q. Yang, *J Am Chem Soc*, 2011, **133**, 20692-20695.
14. A. Cuadras and O. Kanoun, *2009 6th International Multi-Conference on Systems, Signals and Devices, Vols 1 and 2*, 2009, 991-995.
15. D. H. Wang, D. W. Choi, Z. G. Yang, V. V. Viswanathan, Z. M. Nie, C. M. Wang, Y. J. Song, J. G. Zhang and J. Liu, *Chem Mater*, 2008, **20**, 3435-3442.
16. M. C. Yang, Y. Y. Lee, B. Xu, K. Powers and Y. S. Meng, *J Power Sources*, 2012, **207**, 166-172.
17. D. H. Lee, J. G. Park, K. J. Choi, H. J. Choi and D. W. Kim, *Eur J Inorg Chem*, 2008, 878-882.
18. Z. Y. Guo, X. L. Dong, D. D. Zhou, Y. J. Du, Y. G. Wang and Y. Y. Xia, *Rsc Adv*, 2013, **3**, 3352-3358.
19. Y. Ren, Z. Liu, F. Pourpoint, A. R. Armstrong, C. P. Grey and P. G. Bruce, *Angew Chem Int Edit*, 2012, **51**, 2164-2167.
20. W. Q. Han and X. L. Wang, *Appl Phys Lett*, 2010, **97**.
21. B. Hao, Y. Yan, X. B. Wang and G. Chen, *Acs Appl Mater Inter*, 2013, **5**, 6285-6291.
22. Y. S. Hu, L. Kienle, Y. G. Guo and J. Maier, *Adv Mater*, 2006, **18**, 1421-1426.
23. Z. X. Yang, G. D. Du, Q. Meng, Z. P. Guo, X. B. Yu, Z. X. Chen, T. L. Guo and R. Zeng, *J Mater Chem*, 2012, **22**, 5848-5854.
24. P. C. Chen, M. C. Tsai, H. C. Chen, I. N. Lin, H. S. Sheu, Y. S. Lin, J. G. Duh, H. T. Chiu and C. Y. Lee, *J Mater Chem*, 2012, **22**, 5349-5355.
25. Y. D. Wang, B. M. Smarsly and I. Djerdj, *Chem Mater*, 2010, **22**, 6624-6631.
26. Y. D. Wang, T. Chen and Q. Y. Mu, *J Mater Chem*, 2011, **21**, 6006-6013.
27. Z. Ali, S. N. Cha, J. I. Sohn, I. Shakir, C. Yan, J. M. Kim and D. J. Kang, *J Mater Chem*, 2012, **22**, 17625-17629.
28. H. Han, T. Song, J. Y. Bae, L. F. Nazar, H. Kim and U. Paik, *Energ Environ Sci*, 2011, **4**, 4532-4536.
29. J. W. Xu, Y. F. Wang, Z. H. Li and W. Zhang, *J Power Sources*, 2008, **175**, 903-908.
30. E. Ventosa, W. Xia, S. Klink, F. La Mantia, B. Mei, M. Muhler and W. Schuhmann, *Chem-Eur J*, 2013, **19**, 14194-14199.
31. N. A. Kyeremateng, F. Vacandio, M. T. Sougrati, H. Martinez, J. C. Jumas, P. Knauth and T. Djenizian, *J Power Sources*, 2013, **224**, 269-277.
32. J. G. Kim, D. Q. Shi, K. J. Kong, Y. U. Heo, J. H. Kim, M. R. Jo, Y. C. Lee, Y. M. Kang and S. X. Dou, *Acs Appl Mater Inter*, 2013, **5**, 691-696.
33. V. Stengl, V. Houskova, S. Bakardjieva and N. Murafa, *Acs Appl Mater Inter*, 2010, **2**, 575-580.
34. H. J. Tian, L. H. Hu, C. N. Zhang, S. H. Chen, J. A. Sheng, L. Mo, W. Q. Liu and S. Y. Dai, *J Mater Chem*, 2011, **21**, 863-868.
35. N. O. Gopal, H. H. Lo and S. C. Ke, *Journal of the American Chemical Society*, 2008, **130**, 2760-+.
36. Blumenth.Rn, J. Baukus and W. M. Hirth, *J Electrochem Soc*, 1967, **114**, 172.
37. J. Weidmann, T. Dittrich, E. Konstantinova, I. Lauer mann, I. Uhlendorf and F. Koch, *Solar Energy Materials and Solar Cells*, 1999, **56**, 153-165.
38. Y. Y. Li, J. P. Liu and Z. J. Jia, *Materials Letters*, 2006, **60**, 1753-1757.
39. G. Kresse and J. Hafner, *Phys Rev B*, 1993, **48**, 13115-13118.
40. G. Kresse and J. Hafner, *Phys Rev B*, 1994, **49**, 14251-14269.
41. G. Kresse and J. Furthmuller, *Comp Mater Sci*, 1996, **6**, 15-50.
42. J. P. Perdew, K. Burke and M. Ernzerhof, *Phys Rev Lett*, 1996, **77**, 3865-3868.
43. W. Zhao, W. H. Ma, C. C. Chen, J. C. Zhao and Z. G. Shuai, *J Am Chem Soc*, 2004, **126**, 4782-4783.
44. N. Lu, X. Quan, J. Y. Li, S. Chen, H. T. Yu and G. H. Chen, *J Phys Chem C*, 2007, **111**, 11836-11842.
45. V. Gombac, L. De Rogatis, A. Gasparotto, G. Vicario, T. Montini, D. Barreca, G. Balducci, P. Fornasiero, E. Tondello and M. Graziani, *Chem Phys*, 2007, **339**, 111-123.
46. J. Y. Li, N. Lu, X. Quan, S. Chen and H. M. Zhao, *Ind Eng Chem Res*, 2008, **47**, 3804-3808.
47. J. K. Burdett, T. Hughbanks, G. J. Miller, J. W. Richardson and J. V. Smith, *J Am Chem Soc*, 1987, **109**, 3639-3646.
48. Z. S. Hong, M. D. Wei, T. B. Lan and G. Z. Cao, *Nano Energy*, 2012, **1**, 466-471.
49. P. Kubiak, M. Pfanzelt, J. Geserick, U. Hormann, N. Husing, U. Kaiser and M. Wohlfahrt-Mehrens, *J Power Sources*, 2009, **194**, 1099-1104.
50. E. Baudrin, S. Cassaignon, M. Koesch, J. P. Jolivet, L. Dupont and J. M. Tarascon, *Electrochem Commun*, 2007, **9**, 337-342.
51. S. S. Zhang, K. Xu and T. R. Jow, *Electrochim Acta*, 2004, **49**, 1057-1061.
52. N. Takami, A. Satoh, M. Hara and I. Ohsaki, *J Electrochem Soc*, 1995, **142**, 371-379.
53. H. Liu, C. Li, H. P. Zhang, L. J. Fu, Y. P. Wu and H. Q. Wu, *J Power Sources*, 2006, **159**, 717-720.